Surface alloying and mixing at the Mn/Fe(001) interface: Real-time photoelectron spectroscopy and modified embedded atom simulations

Piero Torelli and Fausto Sirotti*
Laboratoire pour l'Utilisation du Rayonnement Electromagnetique, CNRS-CEA-MESR, Boîte Postale P34, F-91898 Orsay, France

Pietro Ballone
Dipartimento di Fisica and Istituto Nazionale per La Fisica della Materia, Università degli Studi di Messina, Contrada Papardo, I-98166 Messina, Italy

(Received 15 May 2003; revised manuscript received 29 July 2003; published 17 November 2003)

Structural and magnetic properties of thin Mn films on the Fe(001) surface have been investigated by a combination of photoelectron spectroscopy and computer simulation in the temperature range 300 K$\leqslant T \leqslant$750 K. Room-temperature as deposited Mn overlayers are found to be ferromagnetic up to 2.5-monolayer (ML) coverage, with a magnetic moment parallel to that of the iron substrate. The Mn atomic moment decreases with increasing coverage, and thicker samples (4-ML and 4.5-ML coverage) are antiferromagnetic. Photoemission measurements performed while the system temperature is rising at constant rate ($dT/dt \sim 0.5$ K/s) detect the first signs of Mn-Fe interdiffusion at $T=450$ K, and reveal a broad temperature range (610 K$\leqslant T \leqslant$680 K) in which the interface appears to be stable. Interdiffusion resumes at $T \geqslant 680$ K. Molecular dynamics and Monte Carlo simulations allow us to attribute the stability plateau at 610 K$\leqslant T \leqslant$680 K to the formation of a single-layer MnFe surface alloy with a 2×2 unit cell and a checkerboard distribution of Mn and Fe atoms. X-ray-absorption spectroscopy and analysis of the dichroic signal show that the alloy has a ferromagnetic spin structure, collinear with that of the substrate. The magnetic moments of Mn and Fe atoms in the alloy are estimated to be $0.8\mu_B$ and $1.1\mu_B$, respectively.

DOI: 10.1103/PhysRevB.68.205413 PACS number(s): 68.35.Fx, 75.70.Ak, 61.50.Lt, 75.25.+z

I. INTRODUCTION

Transition-metal thin films and multilayers can be prepared in a wide variety of compositions, sizes, and structures by present day crystal-growth techniques, providing a wealth of new and potentially useful systems. Magnetic properties, in particular, are very sensitive to dimensionality and local environment, and display in thin films a range of different structures and coupling strengths much wider than in the bulk.[1]

Manganese overlayers on the Fe(001) surface are among the most extensively studied metallic interfaces,[2] partly because iron is the prototype magnetic material, and partly because Mn has a rich variety of crystal forms and a high magnetic moment ($5\mu_B$) in the gas phase.[3] The high spin of the atomic state was emphasized in early theoretical studies, suggesting that low-dimensional Mn structures (either free clusters[4] isolated in a molecular beam or overlayers[5]) would retain an unusually high magnetic moment of $\sim 4\mu_B$ per atom. Moreover, the antiferromagnetism of the α-Mn phase could revert to a ferromagnetic structure because of low dimensionality and epitaxial strain, thus giving origin to a particularly interesting interface characterized by high surface magnetization.

These expectations have only been partially borne out by experiments and by further theoretical studies, which instead produced a wide range of contrasting results for the structure of Mn overlayers on Fe(001), the size of the magnetic moment for the Mn atoms, their relative orientations as well as their ferromagnetic or antiferromagnetic coupling to the magnetic moment of iron. A generally accepted picture for the growth of Mn on Fe(001) is slowly emerging from the most recent studies, but several quantitative details are still uncertain.

Experimental measures show that Mn grows layer by layer at low coverage, adopting a bct (body-centered tetragonal) structure in registry with the underlying Fe(001) pattern.[6–12] At high coverage the ordered layer by layer growth is lost, and further Mn deposition gives rise to islands. Different experiments, however, disagree on the coverage at which the transition in the growth mode takes place (from 3 ML of Ref. 13 to 13 ML of Ref. 14), and on the geometrical parameters (mainly the c/a ratio of the bct cell) characterizing the Mn structure. These differences reflect the dependence of the results on the growth temperature and velocity, as well as on the crystallographic quality and chemical purity of the substrate.

Perhaps the most detailed experimental view of the Mn/Fe(001) interface is provided by recent scanning tunnel microscope studies,[13,15] reporting structural and electronic information for Mn thin films of up to $\sim$10 ML and growth temperature ranging from 323 K to 473 K. According to this study, the growth mode changes from layer by layer to layers plus islands at a coverage of 3 ML. The Mn planes relax outwards, with an estimated interplanar distance that up to 4 ML depends strongly on coverage, reaching a maximum separation of 1.8 Å at 3 ML. Beyond 4 ML the interplanar distance is constant at 1.65 Å. Deposition at $T=370$ K results in a small amount of Fe atoms intermixing with the first (14% Fe), the second (4% Fe), and the third (2% Fe) Mn layer. A 2×2 reconstruction attributed to Mn-Fe surface alloying was observed on Fe terraces at relatively high temperature and low coverage.

Experimental estimates for the magnetic moment of the

Mn atoms vary from $1\mu_B$ of Ref. 11 to $4.5\mu_B$ of Ref. 16, going through a sequence of intermediate values ($1.7\mu_B$;[12] $3\mu_B$,[9] $4\mu_B$,[7]). Even more uncertain, especially in the limit of low coverages, is the magnetic structure of the Mn overlayer and its coupling with the magnetic moment of the underlying iron substrate. Three different scenarios can be found in literature: (i) an antiferromagnetic Mn layer with two different Mn sites,[7,8,16] (ii) a ferromagnetic Mn monolayer in antiferromagnetic coupling with the substrate; further Mn layers couple antiferromagnetically to the previous one,[9,10] (iii) a ferromagnetic Mn layer magnetized in the same direction as the substrate up to 2–3 ML, becoming antiferromagnetic at higher coverages.[11,12]

Oxygen contamination has been shown to play an important role in the determination of the magnetic coupling between Mn and Fe. According to Ref. 17, clean Mn thin layers are ferromagnetic, with a magnetic moment parallel to that of iron, while oxygen contamination leads to an antiferromagnetic coupling between the Mn layer and the substrate.

From a theoretical point of view, a single Mn adatom on an Fe(001) terrace was predicted to lower its energy by site exchange with an underlying Fe atom.[18,19] Moreover, its spin is antiparallel to that of iron when adsorbed *on* the surface, becoming parallel when it is incorporated into the iron slab. The complete Mn monolayer is predicted to be antiferromagnetic, but the ferromagnetic monolayer in antiferromagnetic coupling to the substrate has very similar energy.[20–23] Other authors predict a layer antiferromagnetic growth, with ferromagnetic coupling between iron and the first Mn layer.[24] More complicated atomic and spin configurations have also been considered,[21,22] including a 2×2 ordered MnFe surface alloy.[23] The structural stability of three-dimensional (3D) metal/Fe(001) interfaces [including Mn/Fe(001)] has been analyzed in detail in Ref. 25, using state of the art density-functional schemes, and exploring all possible collinear spin configurations.

Most of the theoretical studies performed until now assumed a sharp Mn/Fe interface. Experimental results, however, provide evidence of limited mixing even at relatively low growth temperatures.[9,13,26] Despite the obvious interest of this subject, and its relevance for magnetic properties,[27] only a few systematic studies have been devoted to Mn-Fe surface alloys, and, more in general, to the thermal stability of the interface. In addition, the available experimental information is once again rather uncertain. The critical temperature for interdiffusion at the interface, for instance, was estimated at 420 K in Ref. 9, higher than 450 K in Ref. 11, and at 600 K in Ref. 16.

In the present study real-time photoelectron (PE) spectroscopy and atomistic simulation are used together to investigate the evolution of the Mn/Fe(001) interface at various coverages stimulated by a progressive (linear) temperature increase. The primary aim is a systematic search of surface alloys, revealed by persistent features in the photoelectron signature of the interface, and characterized by comparison with simulation results.

Because of its surface sensitivity, and its chemical and site selectivity, photoelectron spectroscopy is the technique of choice for a large number of surface and thin-films studies. Real-time measurements allow the direct identification of many interfacial processes, including the determination of critical temperatures and annealing rates characterizing the stability and evolution of most transition-metal interfaces.

Theoretical models belonging to the embedded atom family[28] provide a reliable and efficient framework to investigate structural and thermal properties of metallic interfaces. These methods are admittedly less accurate and less predictive than fully *ab initio* methods. Moreover, they do not provide explicit information on electronic and magnetic properties. However, their computational efficiency allows the simulation of systems and phenomena whose size or characteristic time scale far exceed the reach of *ab initio* schemes.

Starting from a low-temperature deposition, the experimental results show that interdiffusion reduces the relative Mn weight in the PE intensity above $T=450$ K. An apparent plateau in the temperature dependence of the PE intensity reveals the formation of a peculiar structure at $T=610$ K, whose stability extends up to $T=680$ K. Computer simulations allow us to identify this persistent structure with a 2×2 Mn-Fe surface alloy.

These results are complemented by a discussion of magnetic properties of the interface by photoelectron spectroscopy, and by an extensive investigation by computational methods of the potential-energy surface of the system, and of the Mn-Fe interdiffusion kinetics at the interface.

II. EXPERIMENTAL METHODS

Experiments were performed in ultrahigh vacuum (base pressure better than 4×10^{-10} mbar) on the end station of the SB7 beam line[29] of the SuperACO storage ring at LURE, Orsay. The Fe surfaces were prepared by Ar^+ sputtering and annealing cycles of a [001]-oriented Fe-3% Si single crystal. To avoid the surface segregation of bulk impurities (Si, C, and S) the final sputtering-annealing step was milder than the initial ones. Mn layers have been deposited using high-purity materials evaporated by electron bombardment. A typical deposition rate of 0.2 Å/min was adopted, with pressure remaining below 8×10^{-10} mbar. The thickness of the Mn film was measured by a quartz-crystal oscillator and verified by monitoring the Fe $3p$ and Mn $3p$ photoemission intensities. The purity of the interface was controlled by photoemission. The oxygen surface contamination estimated from the 1s peak is less than 1% of a ML. The surface structure was characterized by low-energy electron-diffraction (LEED) experiments. The epitaxial geometry of the as-deposited Mn layers as well as of the annealed surfaces was demonstrated by the observation of 1×1 LEED patterns, obtained for all surfaces with electrons of about 40 eV kinetic energy.

Photoelectron spectroscopy was performed using a SCIENTA SES 2002 hemispherical analyzer. The two-dimensional detector system was used for real-time experiments with an integration time of 5 s per scan. In order to collect in the same energy window both the Mn $3p$ and Fe $3p$ photoemission peaks, a pass energy for the analyzer of 200 eV was used for fast real-time measurements. Swept spectra were instead recorded with a pass energy of 50 eV. The sample magnetization for dichroism experiments was

provided by a horseshoe electromagnet fixed in contact with the sample. The sample was magnetically saturated by current pulses through the winding of the electromagnet, all spectra were measured in remanence. Linear magnetic dichroism in the angular distribution of photoelectrons (LMDAD) was measured in the chiral geometry described in Ref. 30, obtaining two mirror experiments by reversing the magnetization direction. The magnetization was imposed parallel to the Fe(001) surface and perpendicular to the scattering plane defined by the photon beam and by the photoelectron momentum vector. The LMDAD experiments were performed by reversing the magnetization direction after measuring a complete photoemission spectrum with a total measuring time of less than 5 min. The sample mounting can be rotated around the surface normal in order to align the in-plane magnetization of the sample with the incoming polarized photon beam, while the light polarization can be switched from linear to circular with a polarization rate of about 75%.[29] This configuration with a photon beam incident angle of 45° was used for x-ray-absorption spectroscopy (XAS) and to measure x-ray magnetic circular dichroism (XMCD) spectra by detecting the total electron yield photoemitted from the sample surface. XMCD spectra were measured by reversing the magnetization direction for every value of the photon energy. The XMCD spectra of iron present a magnetic asymmetry of 30% at the L_3 threshold, after correcting for the light polarization and geometrical factors.[31] The application of sum rules to the XMCD spectra of iron leads to a value of $2.1\mu_B$ for the magnetic moment, confirming the full magnetization of the iron substrate.

The maximum Fe $3p$ LMDAD asymmetry measured on the clean iron surface at 210 eV photon energy is 20%, corresponding to complete magnetic ordering of the surface. No significant change in the asymmetry was observed upon Mn deposition, suggesting that the growth of the Mn layer induces only small modifications in the magnetic moment and magnetic alignment of the Fe atoms at the interface.

The annealing was driven by a gradual increase of the power applied to a filament mounted on the back of the sample, leading to a constant rate temperature raise. The sample temperature was measured with a Chromel Alumel thermocouple fixed on a sample side.

III. EXPERIMENTAL RESULTS

A. Electronic structure and magnetic properties of as-deposited Mn overlayers

Manganese overlayers on the Fe(001) surface have been prepared at room temperature for coverages ranging from 0.5 ML to 4.5 ML. The LEED patterns for different coverages are almost identical to the ones of the substrate, only the size of the spots is slightly increased at the highest coverages (i.e., 2.5 and 4.5 ML). Then, samples have been characterized by XAS with circularly polarized synchrotron radiation at the $L_{2,3}$ edges of iron and manganese, and by photoemission experiments with linearly polarized radiation on iron and manganese $3p$ core levels and valence bands. Spectra recorded upon reversing the sample magnetization direction have been used to obtain XMCD and LMDAD dichroic signals. The photoemission spectra were taken at 210 eV photon energy. This relatively low photon energy was selected to increase the surface sensitivity and to prevent strong photoelectron-diffraction effects at normal emission for the Fe(001) surface.[32] The Mn overlayer thickness was recalculated using the Mn and Fe $3p$ photoemission intensities assuming in both cases a mean free path of 5 Å.

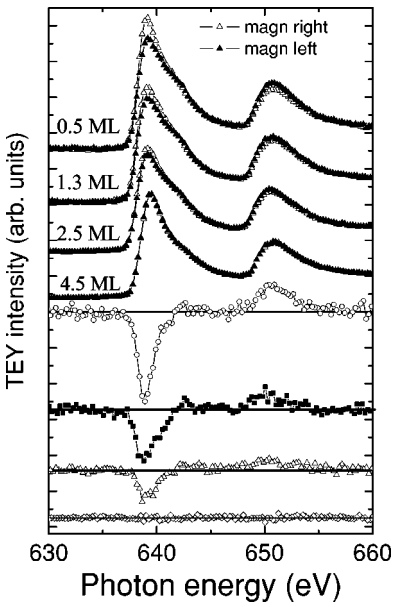

FIG. 1. Manganese $L_{2,3}$ absorption edges measured in total electron yield for four different Mn coverages (0.5 ML, 1.3 ML, 2.5 ML, 4.5 ML). Two spectra with opposite magnetization direction are recorded for each sample and normalized to the same Mn amount using a multiplicative factor. The corresponding XMCD difference spectra (multiplied by a factor of 5) are shown at the bottom of the figure.

The $L_{2,3}$ absorption edges of Mn obtained by reversing the magnetization direction on the sample are shown in Fig. 1 for four Mn coverages, i.e., 0.5, 1.3, 2.5, and 4.5 ML. The spectra are normalized to a constant steplike background corresponding to the same Mn amount, accounting for the transition to the continuum. The smooth line shape, typical of the metallic state,[11] is apparent, although a shoulder on the high photon energy side of the L_3 white line is clearly visible up to 2.5-ML coverage, and a faint shoulderlike feature might be seen in the results for 4.5 ML.

The XMCD signal points to the presence of a net magnetic moment in the Mn layer up to 2.5 ML, the sign of XMCD confirming the ferromagnetic coupling between the iron substrate and the Mn overlayer.[11]

The maximum XMCD asymmetry corrected for geometrical factors and for the light polarization rate is reported in Fig. 2 (lower panel) as a function of Mn coverage. The magnetic signal drops by more than 20% at submonolayer coverages, then it decreases gradually with increasing film thickness, vanishing at 4.5 ML. A similar behavior is observed for the amplitude of the LMDAD signal measured on the same samples.

The XMCD information on the ferromagnetic behavior of the Mn layers is complemented by the analysis of the

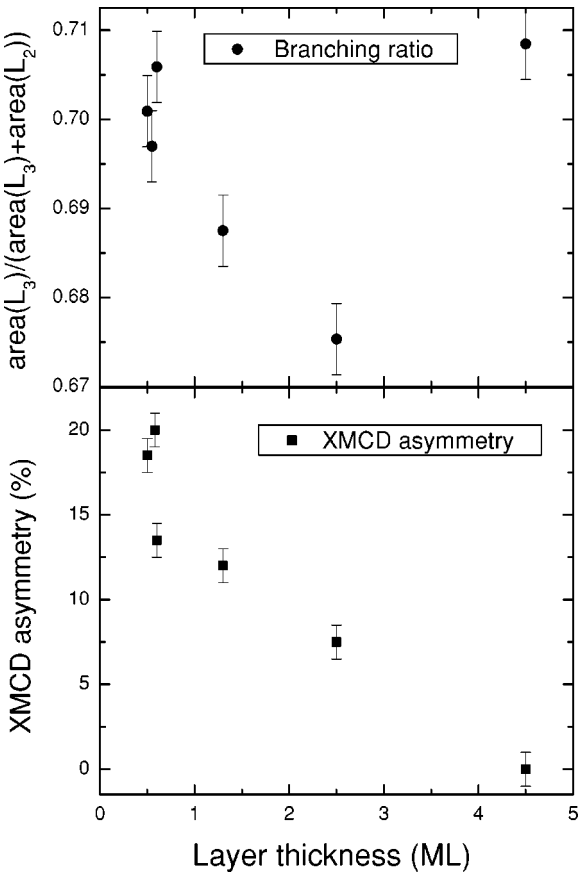

FIG. 2. Branching ratio (top) and maximum XMCD asymmetry (bottom) measured on the Mn $L_{2,3}$ absorption spectra as a function of Mn coverage.

branching ratio in the total relative intensities of the L_3 and L_2 absorption edges calculated on the same spectra. In transition metals the branching ratio (BR), defined as $BR = I(L_3)/[I(L_2)+I(L_3)]$, shows systematic changes related to different magnetic properties. Deviations of BR from the statistical value are due to initial-state spin-orbit splitting and electrostatic interaction between core holes and valence electrons.[33]

The coverage dependent modifications in the Mn electronic structure have been characterized by computing the branching ratio for the spectrum resulting from the sum of the two dichroic spectra shown in Fig. 1. The BR calculated on the total intensity obtained reversing the magnetization direction is not affected by modifications in the alignment between sample magnetization and light polarization, but shows modifications in the spin and total angular momentum.[33] The small spin-orbit splitting of the Mn $2p$ shell is not sufficient to separate the L_3 and L_2 thresholds. The determination of the relative L_2 and L_3 intensity, therefore, is not unambiguous, and has to rely on a suitable definition for the overlapping peaks and on specific choices for the corresponding background. We subtracted a double steplike function, representing transitions to the *s* states, in which the step behind L_2 is half the step of L_3. This procedure will result in an underestimation of the true BR value due to the transfer of L_3 intensity under the L_2 absorption edge. Different background subtraction procedures can change significantly the estimate of the BR, but leave unchanged its relative variations due to changing conditions of the sample. Therefore the resulting values are significant for the discussion. They are reported in Fig. 2 (top panel) as a function of Mn coverage. The behavior of BR is similar to that of the XMCD signal at low coverage, decreasing monotonically up to 2.5 ML. The parallel reduction of XMCD and branching ratio was already observed up to a coverage of 3 ML in Ref. 16, although in that case the Mn layers were characterized by an antiparallel magnetic coupling with the Fe(001) substrate, in contrast with our results. The same coverage dependence of the $L_{2,3}$ branching ratio was observed (up to about 4 ML) for a different Mn-Fe interface, i.e., Mn/Fe(110),[34] and for Mn layers deposited on copper surfaces.[35] The Mn/Fe(110) interface, in particular, displays both a parallel coupling of the magnetic moments and a progressive decrease of BR with increasing coverage.[34] The parallel reduction of the XMCD signal and of the BR in the low coverage range might suggest that the XMCD variation is due to a reduction of the Mn magnetic moment and not simply to magnetic disorder or to the formation of an antiferromagnetic layer. However, the relation between branching ratio and magnetic moment is not unique, since modifications in the electrostatic interaction of core hole and valence electrons also affect BR.

The 4.5-ML sample is characterized by the vanishing of the XMCD signal and by a strong increase in the BR, pointing to the formation of an antiferromagnetic phase for the Mn film at this coverage. This transition in the magnetic ordering of the Mn layer was already observed at the same critical thickness by spin-polarized electron-energy-loss spectroscopy.[9]

Turning now to spectroscopic features, we observe that the line shape of the L_3 absorption edge is modified for Mn layer thickness higher than 4 ML. The shoulder on the high-energy side is no more visible in the thicker samples. The structural transition (vertical relaxation and islands vs layer by layer growth) induces important modifications in the electronic configuration of manganese.

B. Interface reaction kinetics

The thermal stability and behavior of Mn/Fe(001) interfaces at different coverages have been investigated by real-time photoelectron spectroscopy performed while the temperature of the sample was raising linearly in time at the relatively slow rate of $\sim$0.5 K/s. The photoelectron intensity in the kinetic-energy region of the Mn and Fe $3p$ core levels is reported in Fig. 3 as a function of the annealing temperature ($400 \leqslant T \leqslant 730$ K) and of the photoelectron kinetic energy. More precisely, the results in Fig. 3 were obtained for a 4-ML-thick Mn layer with a temperature variation rate of 34 K/min, at a photon energy of 210 eV. The figure shows the progressive reduction of the Mn $3p$ peak intensity and the corresponding increase of the Fe $3p$ peak starting at 400 K. After a first variation, the Fe and Mn peak intensities remain constant for a few minutes while the temperature is still increasing from 600 K to 680 K. New modifications of the

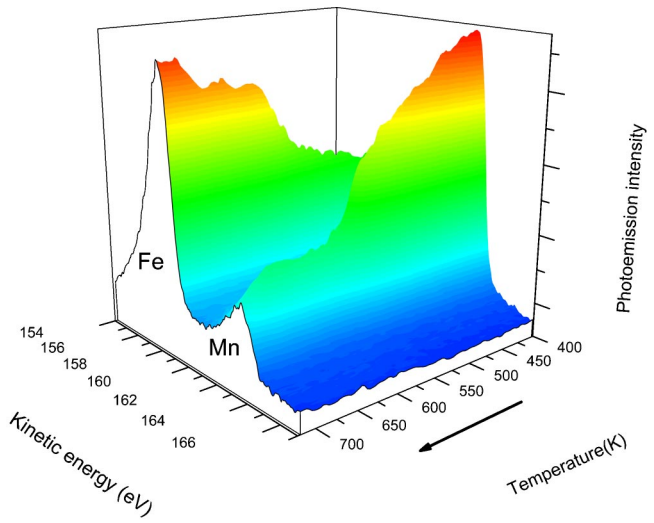

FIG. 3. Photoemission spectra obtained with a photon energy of 210 eV in the kinetic-energy region corresponding to the Fe and Mn $3p$ core levels as measured in real time as a function of the sample temperature in the region from 400 K to 730 K. The heating rate was of 34 K/min and each photoemission spectrum was measured in 5 s with the parallel detection of the electron energy analyzer.

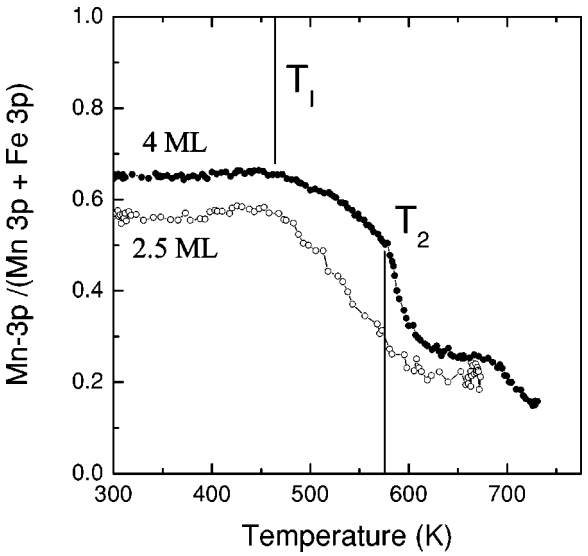

FIG. 4. Relative intensity of the Mn $3p$ peak as a function of temperature measured during the sample annealing for two different coverage of Mn on Fe(001) surface: 4-ML Mn (solid symbols) and 2.5 ML (open symbols).

spectral intensity appear at higher temperature with a reduction of the Mn $3p$ peak and a corresponding increase of the Fe $3p$.

The modifications in the individual intensities of either Fe or Mn can reflect both changes in the system configuration and, to a lesser extent, fluctuations and drifts in the total measured intensity due to the heating process. The interface stoichiometry is measured directly by the relative intensity of the Mn $3p$ peak with respect to the total intensity of the Mn $3p$ and Fe $3p$ photoemission peaks. This identification of relative intensity and composition is made possible by the nearly identical cross section[36] of Fe (0.895) and Mn (0.897) at 210 eV. The results for the Mn relative intensity are reported in Fig. 4 for the experimental data of Fig. 3 and for a lower Mn coverage of 2.5 ML. No modification in the interface composition is observed below the temperature $T_1 \sim 450$ K (see Fig. 4). The relative Mn intensity reduces with temperature increasing from 450 K to 610 K, indicating that interdiffusion is taking place at the interface. It remains constant for $610 \leqslant T \leqslant 680$ K, indicating that a stable atomic configuration has formed at the interface.

The annealing process of a thinner layer (2.5 ML, also shown in Fig. 4) was suspended at $T = 670$ K to study the room temperature magnetic properties of the surface alloy, which will be presented in the last section. A LEED measurement performed after the annealing displays again a 1×1 pattern. This result indicates that the original epitaxial geometry of the Mn overlayer survives to the interdiffusion process observed during the thermal cycle and Fe atoms replace the Mn ones at the surface. The LEED contrast of Mn and Fe atoms is weak, and therefore the observation of a 1×1 LEED pattern does not rule out some degree of order for the surface Mn-Fe configuration, especially if it does not extend to long range. In fact, as anticipated in the Introduction, simulations point to the formation of a 2×2 Mn-Fe surface alloy, whose order, however, is limited to short range (up to ~ 10 Å).

Photoemission intensity alone does not uniquely determine the Mn and /or Fe depth profiles. The 24% Mn $3p$ relative intensity measured at the stability plateau can be obtained for two limiting situations for the annealed sample: (1) all the Mn atoms are incorporated into a surface MnFe alloy having a step profile; (2) a residual Mn layer resides at the surface, while a fraction of the Mn atoms migrate deep into the surface. In this last case the Mn coverage of the surface layer corresponds to about half a monolayer. XAS and photoemission techniques are element specific, and are characterized by a different probing depth. X-ray-absorption spectroscopy in total electron yield detection mode probes several nanometers, while x-ray photoelectron spectroscopy is characterized by a mean free path of few angstroms for kinetic energies of about 100 eV. The relatively higher probing depth of x-ray-absorption spectroscopy in total electron yield with respect to photoemission allow us to discriminate between the two scenarios. The x-ray-absorption spectra performed on the annealed interface showed a strong reduction of the Mn-$L_{2,3}$ signal to 25% of the one obtained from the as-deposited interface. This indicates a strong dilution of about 1.9 ML of the initial 2.5 ML in the Fe substrate. The annealing of Mn layers on the Fe(100) surface in the temperature range $610 \leqslant T \leqslant 680$ K results in the formation of a Mn/Fe surface alloy where half a monolayer of Fe surface atoms are replaced by Mn atoms. The other Mn atoms migrate deeply into the Fe substrate.

IV. THE COMPUTATIONAL MODEL

The temperature evolution of the Mn/Fe(001) interface has been investigated by classical simulation based on a modified embedded atom potential. The starting point is pro-

vided by the well-known embedded atom model,[28] in which atoms interact with their neighbors by a short-range, repulsive pair potential $\varphi(R)$, and gain cohesive energy by being immersed in the pool of delocalized valence electrons:

$$E_{pot}[\{\mathbf{R_I}\},I=1,N]=\frac{1}{2}\sum_{I\neq J}^{N}\varphi_{I,J}(|\mathbf{R_I}-\mathbf{R_J}|)+\sum_{I}^{N}F_I[\rho(\mathbf{R_I})]. \tag{1}$$

In the equation above, E_{pot} is the system potential energy as a function of the atomic coordinates $[\{\mathbf{R_I}\},I=1,N]$, N is the number of atoms, $\varphi_{I,J}(R)$ is the (usually repulsive) pair potential, dependent on the (I,J) atom type, $\rho(\mathbf{R_I})$ is the embedding electron density at position $\mathbf{R}$, and $F_I[\rho(\mathbf{R})]$ is the corresponding energy gain for an atom of type I in the embedding density $\rho(\mathbf{R})$. In turn, the embedding density of each atom is the sum of the contributions from its neighbors:

$$\rho(\mathbf{R_I})=\sum_{J\neq I}^{N}\rho_J^{(0)}(|\mathbf{R_I}-\mathbf{R_J}|), \tag{2}$$

where $\rho_J^{(0)}(R)$ represents the tail of the (spherical) electron density of atom J overlapping with atom I.

This simple model is very successful for metals at the beginning and at the end of the transition series,[37,38] but it is unable to describe the complex structure of manganese, and also for bcc iron its reliability is somewhat limited, although good results have been obtained with special implementations of the embedded atom model (EAM) scheme.[39]

For these reasons, we resorted to a modified embedded atom scheme, in which the potential energy is given by

$$\begin{aligned}E_{pot}[\{\mathbf{R_I}\},I=1,N]=&\frac{1}{2}\sum_{I\neq J}^{N}\varphi_{I,J}(|\mathbf{R_I}-\mathbf{R_J}|)+\sum_{I}^{N}F_I[\rho(\mathbf{R_I})]\\&+\frac{1}{2}\sum_{I}^{N}\frac{t_I^{(1)}[\rho_I^{(1)}]^2}{1+s_I^{(1)}[\rho_I^{(1)}]^2}\\&+\frac{1}{2}\sum_{I}^{N}\frac{t_I^{(2)}[\rho_I^{(2)}]^2}{1+s_I^{(2)}[\rho_I^{(2)}]^2}\\&+\frac{1}{2}\sum_{I}^{N}\frac{t_I^{(3)}[\rho_I^{(3)}]^2}{1+s_I^{(3)}[\rho_I^{(3)}]^2},\end{aligned} \tag{3}$$

where terms accounting for dipole, quadrupole, and octupole deformations of the embedding density around each atom have been added to the basic EAM energy expression. More precisely

$$[\rho_I^{(1)}]^2=\sum_{\alpha}\left[\sum_{I\neq J}^{N}\frac{R_{IJ}^{\alpha}}{R_{IJ}}\rho_J^{(1)}(|\mathbf{R_I}-\mathbf{R_J}|)\right]^2, \tag{4}$$

$$\begin{aligned}[\rho_I^{(2)}]^2=&\sum_{\alpha,\beta}\left[\sum_{I\neq J}^{N}\frac{R_{IJ}^{\alpha}R_{IJ}^{\beta}}{R_{IJ}^2}\rho_J^{(2)}(|\mathbf{R_I}-\mathbf{R_J}|)\right]^2\\&-\frac{1}{3}\left[\sum_{I\neq J}^{N}\rho_J^{(2)}(|\mathbf{R_I}-\mathbf{R_J}|)\right]^2,\end{aligned} \tag{5}$$

$$[\rho_I^{(3)}]^2=\sum_{\alpha,\beta\gamma}\left[\sum_{I\neq J}^{N}\frac{R_{IJ}^{\alpha}R_{IJ}^{\beta}R_{IJ}^{\gamma}}{R_{IJ}^3}\rho_J^{(3)}(|\mathbf{R_I}-\mathbf{R_J}|)\right]^2. \tag{6}$$

In the equations above, α, β, and γ are Cartesian coordinate indices, $\mathbf{R_{IJ}}=\mathbf{R_I}-\mathbf{R_J}$, and $\rho_J^{(1)}$, $\rho_J^{(2)}$, $\rho_J^{(3)}$ are short-range functions similar to $\rho_J^{(0)}$ of the EAM scheme.

The present model is a slight variant of the modified embedded atom scheme introduced in Ref. 40, and already used successfully to reproduce the behavior of metals whose phase diagram is characterized by the competition of several structures, some of them displaying distorted geometries with many atoms in the unit cell.[41] The relation of our model with the standard modified embedded atom method (MEAM) and other models will be discussed in detail elsewhere, while the parametrization of the potential for the Mn/Fe(001) system is described in the Appendix.

V. THE SIMULATION METHOD

The MEAM potential described in the preceding section and in the Appendix has been used to simulate the temperature evolution of the Mn/Fe(001) interface using both Monte Carlo (MC) and molecular-dynamics (MD) algorithms.[42]

The simulated system consists primarily of a α-Fe slab exposing two (001) surfaces perpendicular to the z direction. The surfaces extend over 7×7 bcc conventional unit cells, thus corresponding to a surface cross section of 49 Fe atoms. The simulation cell is periodically repeated in the (xy) plane. The 2D vectors defining the surface periodicity in the xy plane are treated as dynamical variables both in MC and in MD, and the simulation is performed in the N-P-T ensemble with $P=0$. In the z direction, we consider 29 iron planes, and the system thus contains a total of 1421 Fe atoms.

Molecular dynamics, in particular, has been used to relax atomic positions of the interface at different values of Mn coverage, and to investigate the real-time dynamics of the system. Energy optimization has been performed by quenched MD, i.e., by evolving the system in time by MD, and setting all velocities to zero whenever the $3N$-dimensional (N being the total number of atoms) scalar product of velocities and forces becomes negative. In this way, the energy of the system decreases monotonically, and the optimization ends up in the local minimum closest to the starting configuration. The optimization is terminated when the modulus of the largest force on the atoms is less than 10^{-4} eV/Å. A similar strategy is used to optimize the 2D simulation cell of the surface.

The integration of the MD equations of motion is performed by the velocity Verlet algorithm with a time step of 7.6×10^{-15} s.

The time span covered by MD can be extended, at most, to about 100 ns, that is, far too short to approach equilibrium if that requires atomic diffusion in the solid state. The kinetic bottleneck is to a large extent avoided by resorting to MC, including moves that interchange the position of Fe-Mn atom pairs.[43] In this way, atoms are displaced without ever sampling the top of the diffusion barrier. A residual barrier re-

TABLE I. Interplanar distances d(Å) and standard deviations δz(Å) of the z coordinate of atomic planes at the Mn/Fe(001) interface as a function of coverage from 0 to 10 ML. For both Fe and Mn, the index identifying the layers is set to 1 at the Fe/Mn interface, and grows in moving away from the interface on either sides.

Plane	0 ML	1 ML	2 ML	3 ML	4 ML	5 ML	7 ML	10 ML
$d(Fe^3\text{-}Fe^2)$	1.442	1.455	1.464	1.459	1.456	1.458	1.459	1.456
$\delta z(Fe^2)$	0.000	0.000	0.000	0.000	0.038	0.021	0.023	0.041
$d(Fe^2\text{-}Fe^1)$	1.453	1.366	1.357	1.359	1.407	1.373	1.375	1.370
$\delta z(Fe^1)$	0.000	0.000	0.000	0.000	0.059	0.045	0.048	0.061
$d(Fe^1\text{-}Mn^1)$		1.664	1.411	1.375	1.454	1.384	1.389	1.389
$\delta z(Mn^1)$		0.000	0.000	0.000	0.079	0.054	0.056	0.057
$d(Mn^2\text{-}Mn^1)$			1.742	1.627	1.300	1.663	1.669	1.677
$\delta z(Mn^2)$			0.000	0.000	0.039	0.061	0.072	0.066
$d(Mn^3\text{-}Mn^2)$				1.893	1.508	1.442	1.438	1.464
$\delta z(Mn^2)$				0.000	0.104	0.171	0.201	0.164
$d(Mn^4\text{-}Mn^3)$					1.816	1.396	1.450	1.423
$\delta z(Mn^4)$					0.116	0.084	0.147	0.202
$d(Mn^5\text{-}Mn^4)$						1.748	1.519	1.485
$\delta z(Mn^5)$						0.182	0.196	0.194
$d(Mn^6\text{-}Mn^5)$							1.409	1.515
$\delta z(Mn^6)$							0.152	0.209
$d(Mn^7\text{-}Mn^6)$							1.751	1.472
$\delta z(Mn^7)$							0.214	0.212
$d(Mn^{10}\text{-}Mn^9)$								1.771
$\delta z(Mn^{10})$								0.222

mains, due to the fact that atomic positions are swapped discontinuously, i.e., without relaxing the coordinates of the neighboring atoms. Nevertheless, this algorithm allows the system to reach equilibrium over most of the temperatures ($100 \leqslant T \leqslant 800$ K) of interest for the present study.

Information on the real-time evolution of the system is partly recovered by interpreting the atom pair interchanges according to a (simplified version of) kinetic Monte Carlo algorithm,[44] as described below.

VI. MEAM PREDICTIONS FOR THE STRUCTURE OF Mn OVERLAYERS

As a first step, we determine the equilibrium geometries and absorption energies for Mn/Fe(001) as a function of coverage, from the isolated Mn adatom to 10 ML. As already discussed in the Introduction, experimental results show that at low coverage Mn grows layer by layer, adopting a bct structure in registry with the underlying Fe(001) pattern. At high coverage the ordered layer by layer growth is lost, and further Mn deposition gives rise to islands. Different experiments, however, disagree on the coverage at which the transition in the growth mode takes place, and also provide different estimates of the c/a ratio of the bct unit cell. Nevertheless, most of the experiments report large variations with coverage of the Fe-Mn and Mn-Mn interlayer separations, with an anomalous increase of the interlayer Mn-Mn distance $d_{\text{Mn-Mn}}$ (up to 1.85 Å) approaching the layer by layer to islands transition, followed by a stabilization at $d_{\text{Mn-Mn}} \sim 1.65$ Å when growth is no longer planar.

Qualitatively similar features are apparent also in the MEAM results, which are summarized in Table I. All structures have been obtained by relaxing the atomic positions starting from an initial bcc structure at the Fe lattice parameter, with n_{Mn} full manganese planes epitaxially adjusted to the underlying iron lattice. We anticipate, however, that the results of this section change significantly (bringing them closer to the experimental findings) if even limited disorder is introduced at the interface, for instance, by exchanging a few Mn-Fe pairs (less than 10% of a ML) in adjacent planes.

Up to 5 ML, complete (001) Mn overlayers do not display in-plane relaxation. Beyond this coverage, a small in-plane relaxation is apparent, but (in-plane) displacements from the ideal positions remain below 0.02 Å. The relaxation of Mn along z, instead, is always significant, and displays a complex pattern. The ideal bcc planes assumed at the beginning of the geometry optimization remain exactly planar up to 3-ML coverage. Starting from 4 ML, the atoms initially belonging to the same (001) plane end up with different optimized z coordinates, as shown by the nonvanishing δz parameter of Table I.

The topmost Mn layer (which is planar up to 3 ML, and only approximately planar at higher coverage) displays a large outward relaxation, with an interlayer separation reaching a maximum of 1.893 Å at 3 ML. Both the loss of planarity and the anomalously high interlayer separation point to an incipient instability of the pseudomorphic growth observed at low coverage. Beyond 3 ML, the change of structure revealed by the corrugation of the Mn planes reduces the separation of the topmost Mn layers to ~ 1.75 Å. At high coverage, the sequence of Mn-Mn interlayer separations displays wide oscillations in going from the surface to the

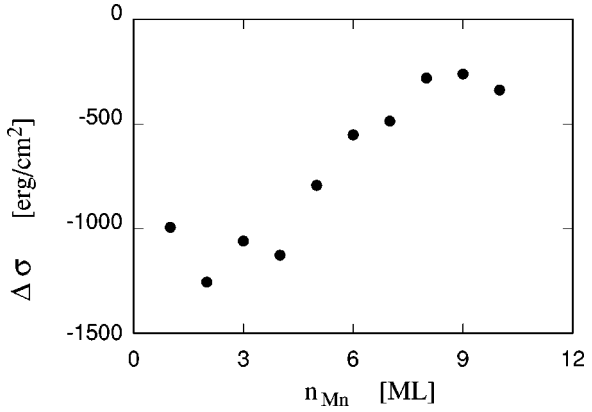

FIG. 5. Energy difference (per unit area) between a relaxed Mn/Fe(001) slab at n_{Mn} manganese coverage and a reference system made by a relaxed Fe(001) slab, and by ($n_{\mathrm{Mn}}\times M_{\mathrm{Mn}}$) Mn atoms in their ground-state α-Mn phase (see text). N_{Mn} is the number of atoms per plane, and the cohesive energy of α-Mn is 2.902 eV per atom.

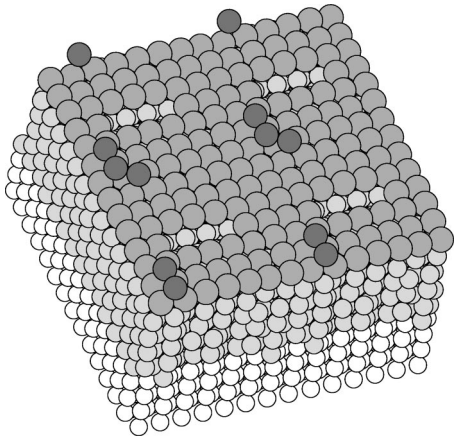

FIG. 6. Structure of a Mn/Fe(001) sample at 10-ML coverage, after a MD run at $T=600$ K lasting 1.5 ns, followed by gradual annealing to $T=100$ K lasting another nanosecond. Iron atoms are white; Mn atoms are gray. Different gray shading have been used to distinguish adatoms (dark gray) and Mn atoms in the topmost layer (middle gray) from all the other Mn atoms (light gray). The simulated sample has been replicated two times in the *x* and *y* direction to highlight the groove structure. Only the topmost planes of the iron slab are shown.

Fe-Mn interface, with, however, a c/a ratio that tends to be >1. The exceptions to the $c/a>1$ rule are found for cases in which a few atoms assume anomalous positions in between planes, making a precise identification of planes somewhat ambiguous. Despite the apparent lateral compression in the Mn overlayer, the Fe-Mn separation at the interface is shorter than in bulk iron at all coverages higher than 1 ML. Also the first Fe-Fe interlayer separation is strongly reduced. Relaxations in the Fe slab are very small beyond the third layer.

The structural trends observed in the Mn overlayers are reflected in the dependence of the system energy on coverage. In our computation, the stability of the overlayers at zero temperature is characterized by the energy difference $\Delta E[n_{\mathrm{Mn}}]$ (where n_{Mn} is the Mn coverage in ML) between the potential energy $E[n_{\mathrm{Mn}}]$ of the optimized samples, and a suitable reference energy, which we define as the sum of the energy $E[\mathrm{Fe}(001)]$ of the relaxed Fe slab, plus the cohesive energy of $n_{\mathrm{Mn}}\times N_{\mathrm{Mn}}$ (N_{Mn} being the number of atoms in each layer, i.e., $N_{\mathrm{Mn}}=49$ in our computations) manganese atoms in the ground-state α-Mn bulk structure:

$$\Delta E[n_{\mathrm{Mn}}]=E[n_{\mathrm{Mn}}]-E[\mathrm{Fe}(001)]-(n_{\mathrm{Mn}}\times N_{\mathrm{Mn}})e_c[\alpha-\mathrm{Mn}], \tag{7}$$

where $e_c[\alpha-\mathrm{Mn}]=2.902$ eV/atom. The resulting energy difference per unit area $\Delta\sigma[n_{\mathrm{Mn}}]$ is shown in Fig. 5. It accounts for the surface energy of the slab and for the Mn/Fe(001) interfacial energy. Both these contributions are n_{Mn} dependent and are difficult to disentangle. The large negative values of $\Delta\sigma[n_{\mathrm{Mn}}]$ at low coverage reflect the lower surface energy of Mn with respect to Fe ($\sigma_{\mathrm{Fe}}=2500$ dyn/cm^2 and $\sigma_{\mathrm{Mn}}=1500$ dyn/cm^2, respectively, as computed by our MEAM model). The reduction of the energy advantage of the interface with respect to the isolated components with increasing coverage is due to the progressive increase in the elastic energy of Mn growing at the in-plane lattice constant of Fe. The crossover between these two regimes takes place at $n_{\mathrm{Mn}}\sim 4$ ML, where the transition to a modulated surface height (i.e., $\delta z\neq 0$) becomes apparent.

To test the local stability of the Mn overlayers, samples at 1-ML, 5-ML, and 10-ML coverage were equilibrated by MD at $T=600$ K. The simulation time (1.5 ns) was too short to result in any Fe-Mn mixing (as will be discussed in the following section). Progressive annealing (lasting slightly longer than 1 ns) down to low temperature ($T\sim 100$ K) followed by quenched MD energy minimization resulted in configurations indistinguishable from the initial ones in the case of the 1-ML and 5-ML samples. In the case of 10-ML coverage, instead, we observe the formation of a few adatom-advacancies pairs, which upon annealing give rise to a short linear groove exposing [011] facets (see Fig. 6), with a corresponding number of adatoms residing on the topmost terrace. The total energy at the end of the annealing is lower than that of the planar sample. This result confirms that a large amount of elastic energy is stored in the flat surface at high coverage, although the simulation time is too short and the system size is far too small to reproduce faithfully the islands' formation process.

In the case of flat interfaces, the roughening of the exposed surface provides the kinetically least demanding route to release strain at high coverage. Another mechanism is present at all coverages >1 ML, which probably plays a far more important role in experimental systems, although its kinetics seems to be far slower in the absence of steps or interfacial vacancies. We verified that interchanging at random a few Mn-Fe atom pairs at the interface decreases the system energy and reduces the oscillations of the interplanar distances at all coverages larger than 1 ML. The strongest effect of interfacial disordering is observed at 3 ML, i.e., immediately before the system releases some strain by breaking the planar symmetry of the Mn layers. The interchange of less than 10% of a ML reduces the interplanar separation between the two topmost planes to 1.69 Å almost indepen-

dently of coverage, in qualitative agreement with several experimental estimates for the interlayer spacing (see Ref. 13).

For completeness, we summarize here the results for a single Mn adatom on the Fe(001) surface. The equilibrium position is given by the bcc site, with an adsorption energy of 3.06 eV. The Mn-Fe nearest-neighbor distance is $\sim 1\%$ shorter than in the full monolayer case. The on-top site is 0.82 eV higher in energy and it is unstable, i.e., it decays to the bcc site by steepest descent energy minimization. Exchange of the Mn adatom in the stable bcc site with one of its Fe nearest neighbors in the surface increases the system energy by 0.16 eV. The interaction of the Mn atom incorporated into the upper surface plane with the Fe adatom is slightly repulsive: the system energy progressively decreases with increasing distance between these two atoms, with an asymptotic energy gain of 0.05 eV. These results are easily rationalized by considering that the Fe-Fe attractive interaction is stronger than the Mn-Fe one. However, the MEAM result for the nearest neighbor interchange energy differs from that obtained by density-functional—Korringa-Kohn-Rostoker (KKR) computations[19] (see also Refs. 18 and 45), predicting a negative exchange energy for Mn on Fe(001). The discrepancy could be due to the fact that magnetism is not explicitly included in our computation, while it is accounted for by the density-functional model. On the other hand, atomic relaxations, included in our computation but neglected in Ref. 19 could also play a role. To quantify this last effect, we repeated our computations by placing all atoms on the ideal bcc lattice at the Fe lattice constant, and recomputing energies without relaxing the atomic positions. We verified that in this way the absorption energy is reduced by less than 10% (from 3.06 eV to 2.80 eV), but the exchange energy changes by more than 50% (from 0.16 eV to 0.07 eV).

VII. MONTE CARLO SIMULATIONS OF Mn-Fe MIXING

The surface segregation or interdiffusion of an adlayer deposited on a surface is determined both by equilibrium and kinetic conditions, with the latter playing at interfaces a far more significant role than in bulk systems. Simple considerations, in particular, show that at any nonvanishing temperature the interface between a bulk crystal and a finite coverage overlayer is only a metastable state, since the diffusion of the adatoms into the (macroscopic) substrate provides an unlimited source of entropy (See Ref. 46 and also Ref. 47). Kinetic constraints, however, often prevent the diffusion of the adatoms into the substrate, or, at least, they limit it to a thin surface layer. This, in turn, reduces somewhat the role of entropy, and opens the way to a variety of localized mixing and surface alloys.

Starting from an ordered Mn overlayer on Fe(001), stability conditions are first investigated by performing a sequence of random Fe-Mn exchanges with restrictions that enforce local mixing. For instance, starting from an ordered Mn monolayer on Fe(001), we progressively exchange Mn atoms in the overlayer with Fe atoms belonging to the last iron plane. The results are shown as solid dots in Fig. 7. Every random exchange raises the system energy, but the dependence of ΔE_x on the Fe concentration of the upper plane is far from linear, as we could expect on the basis of simple surface energy considerations. Instead, the first few exchanges require a relatively low energy (less than 200 K per surface atom for up to 20% mixing), but further interchanges requires a progressively increasing energy.[48]

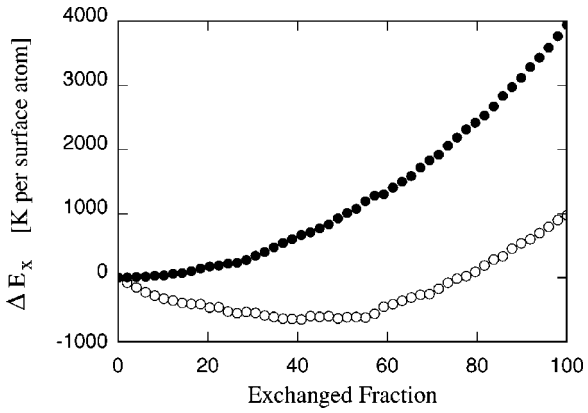

FIG. 7. Energy variation upon random exchanges of Mn atoms with Fe atoms belonging to the topmost iron plane. Exchanges are performed starting from (1) a single monolayer of Mn (solid dots); (2) a 2-ML Mn overlayer (empty circles). In the 2-ML case, the Mn atoms to be exchanged belong to the interfacial (i.e., subsurface) plane (see text). All configurations are relaxed by quenched MD.

The situation is different for the 2-ML coverage. Random interchanges of atom pairs limited to the two (one Fe and one Mn) interfacial planes decreases the system energy up to 50% mixing, i.e., up to random composition of these two interfacial planes (empty circles in Fig. 7). Starting from this optimal configuration, energy raises again if the mixing process is continued, and, even more if interchanges are extended to include Mn atoms belonging to the topmost Mn plane (not shown in Fig. 7).

The depth dependence of the mixing energy has been investigated by moving a single Mn atom from the interfacial plane into progressively deeper Fe planes. The corresponding energy variations are shown in Fig. 8 for the 1-ML and 2-ML coverage. As already apparent from Fig. 7, the diffusion of a Mn atom into the first Fe plane rises slightly the potential energy in the 1-ML case, and releases a substantial amount of energy at 2-ML coverage. Surprisingly, the difference between the 1-ML and 2-ML coverages persists well inside the Fe slab: further diffusion of the Mn atom deeper into the Fe slab is opposed by a rapidly increasing potential-energy function in the 1-ML case, and favored by an even more significant energy gain at 2-ML.

These preliminary results suggest that limited mixing at the interface will not be opposed by a sizable potential-energy raise for coverages $\geqslant 1$ ML, while more extensive (in concentration or depth) mixing might have to overcome increasing energy requirements.

As a further exploration of the energetics of mixing at $T = 0$ K, we computed the energy $\Delta E_{mix}(n_{\mathrm{Fe}}, n_{\mathrm{Mn}})$ required to randomly dissolve n_{Mn} Mn layers into the first n_{Fe} layers of the Fe(001) slab. The reference energy, therefore, is provided by the potential energy of the fully segregated Mn overlayers

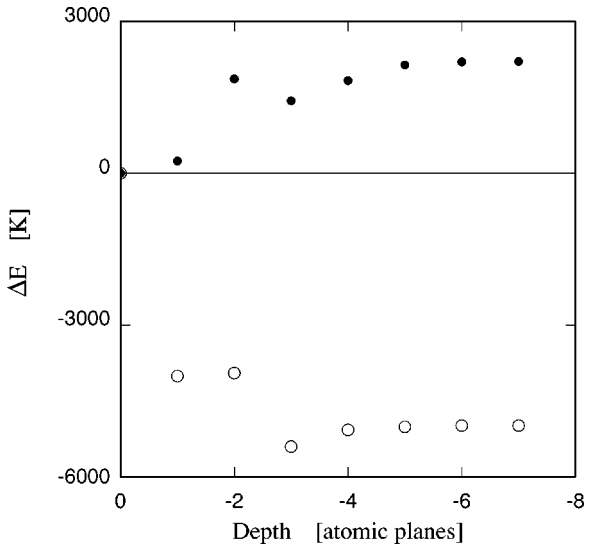

FIG. 8. Energy variation upon interchanging a single Mn atom with Fe atoms belonging to (001) planes at different depth from the surface. The zero of energy and depth corresponds to an ordered Mn overlayer at 1-ML (solid dots) and 2-ML (empty circles) coverage. In the 2-ML case, the interchanged Mn atom belongs to the interfacial (i.e., subsurface) plane. All configurations are relaxed by quenched MD.

discussed in the preceding section. The results for $\Delta E(n_{\mathrm{Fe}},1)$ and $\Delta E(n_{\mathrm{Fe}},2)$ are reported in Fig. 9. As expected, extensive mixing is accompanied by an increase of potential energy, because it exposes Fe surface regions at expense of a Mn surface, whose surface energy is lower. Also in this case, however, the dependence of $\Delta E_{mix}(n_{\mathrm{Fe}},n_{\mathrm{Mn}})$ on either n_{Mn} or n_{Fe} does not follow any simple rule, and displays stability peaks and valleys that could point to surface alloys.

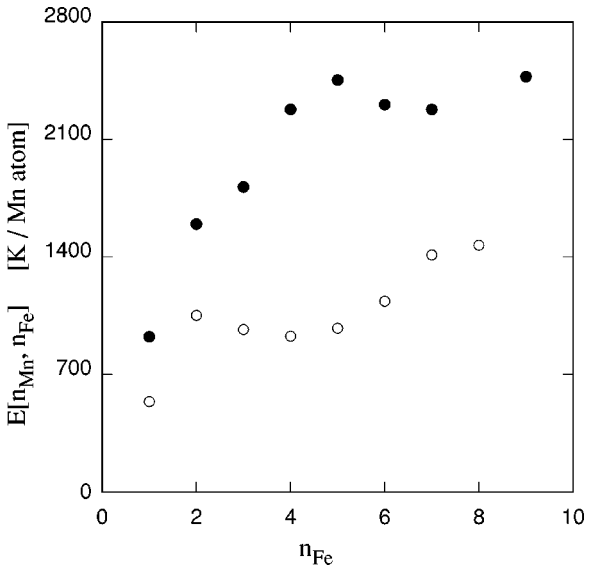

FIG. 9. Energy required to randomly mix n_{Mn} manganese planes with n_{Fe} iron planes starting from a segregated and pseudomorphic Mn overlayer. Solid dots—$n_{\mathrm{Mn}}=1$ ML; empty circles—$n_{\mathrm{Mn}}=2$ ML.

A direct test of thermal stability and kinetics for the Mn/Fe(001) interface was first attempted by molecular dynamics, although it is well known that the time scale of atomistic simulation is usually too short to observe diffusion in the solid state. These computations, therefore, were meant mainly as a test of the global reliability of the model, and provide only an (not very stringent) upper bound for the rate of atomic exchanges at the interface. No diffusion event was observed in any MD simulation, lasting up to 50 ns at temperatures up to 600 K.

To overcome the kinetic barrier preventing the equilibration of the system, we resorted to Monte Carlo. Computations have been done for the 1-ML and 2-ML coverages, starting from the fully segregated state, and covering the $100 \leqslant T \leqslant 800$ K temperature range. To mimic the real-time evolution of the system, atomic exchanges of Fe-Mn atom pairs have been restricted to close neighbors. Since the first and second nearest-neighbor distances are rather close in the bcc structure, while the third neighbors' shell is well separated, we consider only interchanges of nearest and next-nearest neighbors. In other words, the exchange is attempted only for atom pairs whose distance is less than that 3.6 Å.

A simple interpretation of the results in a kinetic MC framework[44] is provided in the following section, under the assumption that pair interchanges within the first two neighboring shells are the leading mechanism for diffusion and mixing. In this section the system evolution is discussed as a function of the number N_x of attempted Fe-Mn pair interchanges, while the time scale of the simulation in real units will be determined *a posteriori* from an estimate (discussed below) of the free-energy barrier for the leading diffusion mechanism. The conversion factor from N_x to real time depends exponentially on the inverse temperature, and we anticipate that the time span of our simulations falls in the macroscopic range for $T \leqslant 400$ K, and in the mesoscopic range ($\sim$ microsecond) at higher temperatures. At all temperatures, however, the time covered by MC is several orders of magnitude longer than what could be achieved by MD.

For 1-ML and 2-ML coverages, the results reflect closely the $T=0$ energy data discussed in Sec. VI. Limited mixing at the interface occurs quickly at all temperatures for the 2-ML case, and at all but the lowest temperatures at 1-ML. The process, however, slows down dramatically after the first few atomic exchanges (especially for the 1-ML case), and extended interdiffusion is observed only at the highest simulated temperatures.

We discuss here in detail the picture emerging after $N_x = 500$ attempted exchanges *per Mn atom*, which, as emphasized above, correspond to a different time interval for the different temperatures. Over this MC-time span, Mn diffusion at 1-ML coverage is limited to the first Fe plane for $T \leqslant 200$ K, and the degree of mixing remains well below 10% during the longest simulations we could perform. Manganese diffusion to deeper planes is observed starting from $T \sim 300$, but up to $T=500$ K most of the Mn atoms remain confined to the three topmost iron planes, with concentrations close to 10%–15%. A few atoms are able to cross the entire iron slab, giving rise to an apparent secondary condensation peak at the opposite free surface of the slab (See Fig.

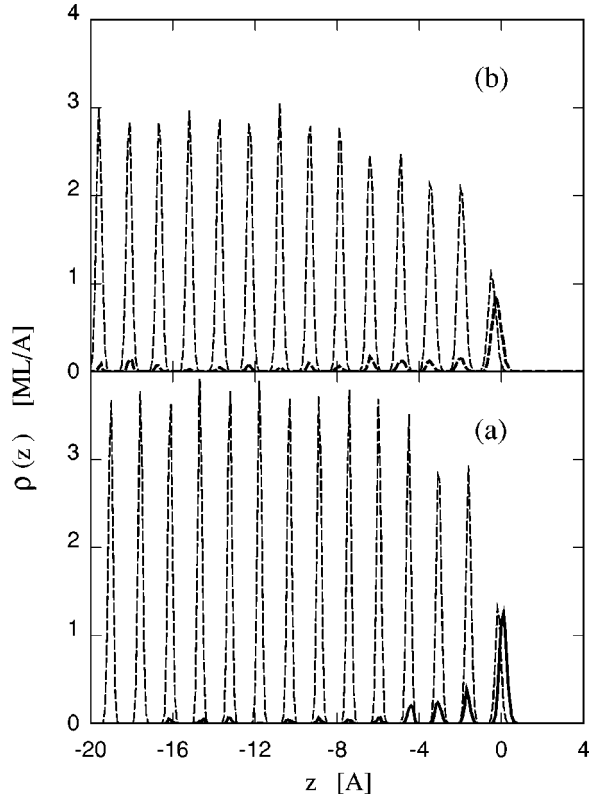

FIG. 10. Density profile of Fe (dash line) and Mn (full line) across the surface at 1-ML manganese coverage after $N_x=500$ attempted exchanges per Mn atom. The zero of the abscissa coincides with the uppermost manganese layer in the starting configuration (fully segregated overlayer). (a) $T=500$ K; (b) $T=800$ K.

10). At $T=500$ K, the Mn concentration in the surface plane (originally 100% Mn) is reduced to 50% after $N_x=500$ attempted exchanges, then remains remarkably constant during much longer simulations. At higher temperatures, the 50% concentration in the upper layer is reached sooner, but then displays a similar stability plateau. Only above $T=700$ K we have been able to observe a decrease of the Mn surface concentration below 50%, but this further stage of mixing appears to be very slow even at $T=800$ K.

Analysis of snapshots shows that the peculiar stability of the 50% concentration for the upper plane is due to the formation of a single-layer 2×2 checkerboard ordered surface alloy.[49] The geometry produced by the simulation is defective both because of the relatively high temperature at which this structure is observed and because of the mismatch of the 7×7 simulation cell and 2×2 unit cell.[50] The similarity of the Fe and Mn atoms and the lack of long-range order imply that this structure would still appear as 1×1 under LEED, unless a careful analysis of intensity and shape of the diffracted spots is performed.

The density profiles found during the simulation at intermediate temperatures or intermediate times are suggestive of a multiphase system, made by a single-crystal plane of FeMn alloy, with a dilute (vaporlike) population of Mn atoms spread around the entire slab, with a disordered (liquidlike) iron-rich solid solution wetting the crystal phase, and extending over three-four atomic planes [see Fig. 10(b)]. We emphasize again that this picture represents only a transient feature, since in the thermodynamic limit the system will necessarily evolve towards the completely mixed state over sufficiently long times.

The evolution of the 2-ML case displays both similarities and differences with the 1-ML coverage. As expected, diffusion of the Mn atoms belonging to the interfacial plane occurs readily at all temperatures, because it decreases the system potential energy, while, at the same time, it increases entropy. Moreover, Mn diffusion progresses deeper than in the 1-ML case, because there is no significant potential energy increase opposing this process. The topmost Mn layer, however, is far more stable than in the 1-ML case, and no iron contamination of this layer is observed for $N_x=500$ at $T\leqslant300$ K. The iron-rich solid solution wetting the topmost layer apparently prevents Fe atoms from reaching the surface. On longer time scales or at higher T, the dissolution of this disordered protective buffer opens the way to intermixing in the top plane. Eventually, the Mn concentration in the top plane reduces to 50%, which represents again a state of relative stability for the system. Also in this case, the stability of the 50% composition for the top layer is due to the formation of a defective 2×2 single-plane FeMn surface alloy. Above $T=700$ K, or for very long simulations, the evolution of the 2-ML coverage is similar to the 1-ML case, ending with the nearly complete dissolution of the Mn overlayer.

The computational results for the time evolution of the overlayer can be summarized by computing the relative photoemission intensity due to Mn ($R_{\mathrm{Mn}}(N_x)=I_{\mathrm{Mn}}(N_x)/[I_{\mathrm{Fe}}(N_x)+I_{\mathrm{Mn}}(N_x)]$) as a function of MC time (measured by N_x) are determined by attributing the same PE cross section to Fe and Mn, and assuming an exponential decay of the intensity from atoms buried below the surface with a mean free path of 5 Å.

The results for the 2-ML coverage are shown in Fig. 11 for $T=650$ K and $T=800$ K. At both temperatures, the time dependence of $R_{\mathrm{Mn}}(N_x)$ cannot be reproduced by a single exponential, and apparently results from the superposition of processes having different time scales. The analysis of snapshots and of concentration profiles allows us to identify the different stages appearing in the R_{Mn} evolution. The initial rapid drop of $R_{\mathrm{Mn}}(N_x)$ ($N_x\leqslant40$) observed at $T=650$ K and $T=800$ K is due to limited diffusion in the Fe-Mn interfacial planes. At $T=650$ K this first stage is followed by the full dissolution of the interfacial Mn plane ($40<N_x\leqslant280$), leaving behind an iron-rich FeMn solid solution wetting the topmost layer. The Mn concentration in this surface plane is reduced to 50% only for $N_x\sim450$. The decay of $R_{\mathrm{Mn}}(N_x)$ continues slowly even beyond this point, but it is due almost exclusively to the progressive decrease of the subsurface Mn population, while the Mn concentration in the topmost layer remains nearly constant at 50%. The evolution is somewhat different at $T=800$ K. In this case, the full dissolution of the interfacial Mn layer and the contamination of the top Mn layer by Fe take place almost simultaneously. A 2×2 FeMn surface alloy is clearly recognizable for $250\leqslant N_x\leqslant750$, but

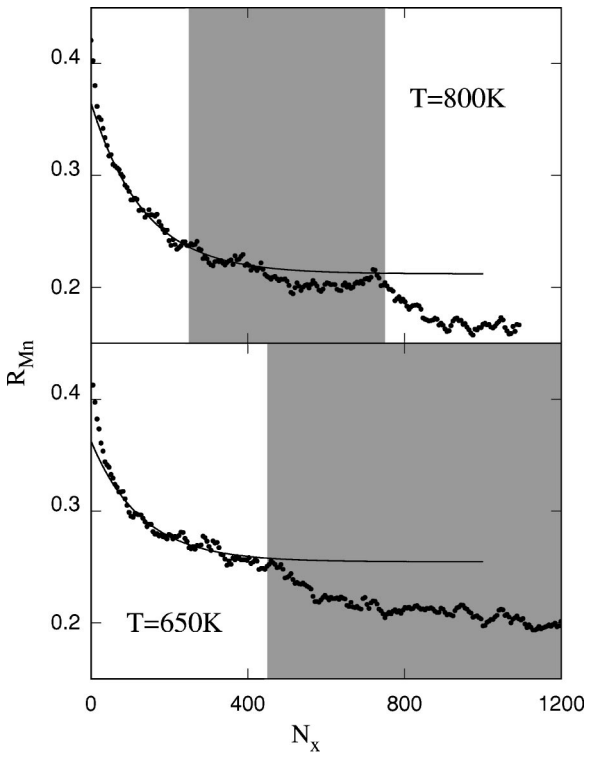

FIG. 11. Relative Mn contribution to the photoemission intensity (see text) from MC simulations as a function of the number N_x of attempted Fe-Mn pair exchanges. The gray area identifies the stability range of the single-layer 2×2 FeMn alloy discussed in the text. The full line is a fit of the $40\leqslant N_x\leqslant 400$ data by a single exponential, suggesting that each curve is the superposition of several exponentials with different decay times.

in this case we also observe the decay of the surface alloy for $N_x\geqslant 750$.

The results presented in Fig. 11 cannot be directly compared with the experimental data of Fig. 4 because the latter are obtained for a uniform temperature scan, while the former display the time evolution of the system at constant temperature. It is nevertheless natural to identify the stability plateau in Fig. 4 with the formation of the FeMn surface alloy found by simulation.

VIII. MEAM ESTIMATE OF THE FREE-ENERGY BARRIER FOR Mn-Fe INTERDIFFUSION

In the preceding section the system evolution has been discussed in terms of the number N_x of attempted Fe-Mn pair interchanges. In this section we estimate the simulation time scale in real units, under the assumption that interchanges between nearest and next-nearest neighbors are the leading mechanism for diffusion.

The correspondence is established by assuming that a pair interchange is attempted every time the system reaches the top of the free-energy barrier separating the original from the exchanged configuration. Therefore, we associate with each interchange attempted by our MC procedure a time span that is the inverse of the estimated frequency at which the system visits the top of the barrier. This assumption, of course, represents a major approximation, but it can be justified within the kinetic Monte Carlo framework.[44]

The probability to reach the top of the barrier for the pair interchange is given by the Arrhenius expression

$$R=\nu e^{-\Delta F_b/K_BT}, \tag{8}$$

where ΔF_b is the free energy required to reach the saddle point and ν is a typical system frequency, which we set to the Debye phonon frequency of Fe ($\nu=10$ THz). Therefore, the time associated with each attempted exchange is

$$\tau=1/R=10^{-13}e^{\Delta F_b/K_BT}, \tag{9}$$

where τ is in seconds.

The free-energy barrier ΔF_b has been computed by a sequence of constrained MD simulations,[51] starting from an ordered sample at 1-ML coverage and $T=300$ K, and ending with the exchanged configuration. The reaction coordinate is represented by the distance δz along the z axis (perpendicular to the surface) between a tagged Mn atom (the one that will be exchanged) and the center of mass of the topmost Fe plane. Because of significant hysteresis close to the barrier top, the ascending and descending portions of the path are sampled independently. In the ascending path, the reaction coordinate progressively reduces from the equilibrium value ($\delta z=1.68$ Å at $T=300$ K) towards the saddle point. The descending path is sampled in a similar way, starting from the exchanged configuration (corresponding to $\delta z=0$) and progressively increasing δz.

The free-energy profile along the reaction path is computed using the method described in Ref. 51. For each value of δz the system is equilibrated for 10 ps, then the generalized force on the constraint is averaged during other 10 ps. The free-energy difference between two points along the reaction path is given by the line integral of the generalized force on the constraint.[51] The ascending and descending portions of the reaction path are joined by assuming that the configurational free-energy difference between the original and exchanged configurations are equal to the corresponding potential-energy difference, thus neglecting the vibrational contribution to the free-energy difference. Because of the similarity in the atomic masses and interatomic potentials of Mn and Fe, the error due to this approximation is probably very small. The same method has been used to estimate the barrier for a second exchange, bringing the Mn atom one further layer within the slab.

The results are shown by solid dots in Fig. 12. The points close to the saddle points are the most affected by uncertainties due to the short simulation time, and for this reason they are not reported in the figure. In a relatively wide range around each of the (local) minima the free-energy profile displays a parabolic behavior, as shown by the continuous lines in Fig. 12. The curvature of the parabolas is nearly the same for the different minima, and, since the free-energy difference among minima is small with respect to the free-energy rise in between, we assume in the following that there is a unique barrier characterizing the diffusion properties of Mn in the Fe slab. This unique free-energy barrier is estimated from the crossing of the parabolic interpolations to be

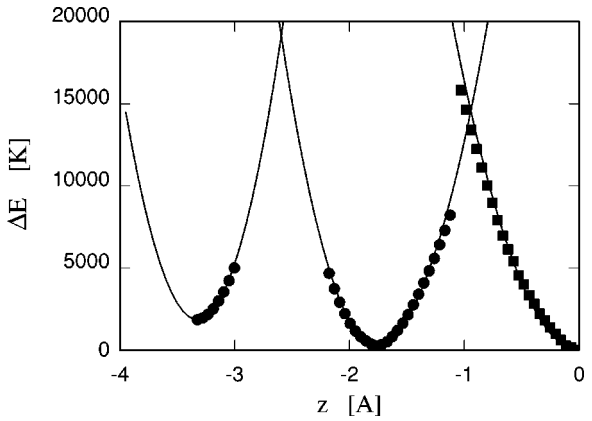

FIG. 12. Free-energy profile for a Mn atom diffusing from the surface towards the interior of a Fe slab. The simulation is performed at $T=300$ K, at 1-ML coverage. Filled squares: free-energy valley for Mn atoms in the overlayer. Solid dots: free-energy valleys for Mn atoms residing in underlayers.

$\Delta F_b = 15\times 10^3$ K, or 1.3 eV. This value probably represents an overestimate of the true barrier, since relaxation mechanisms will reduce the energy and the strength of the interatomic forces for the most strained configurations, rounding the peaks of the free-energy profile. Despite this overestimate, and several other approximations, the present estimate is likely to provide the correct order of magnitude for the free-energy barrier, thus setting the scale of the simulation time in real units. Substitution of ΔF_b into Eq. (9) gives $\tau = 1900$ s for $T=400$, $\tau=1$ s for $T=500$ K, and $\tau=1.4\times 10^{-5}$ s at $T=800$ K.

Computations for the 2-ML case performed using the same method show that the free-energy barrier for exchanging a Mn-Fe pair at the interface is equal to the 1-ML value to within 10%. The similarity of the free-energy barriers for the 1-ML and 2-ML cases might seem surprising, given the significant difference of the exchange energy in the two cases. It becomes less surprising if one takes into account that free-energy barriers are at least two orders of magnitude larger than exchange energies, and apparently they are not much affected by the slight differences in the relative stability of the end points. From these results we conclude that the estimate of the simulation time span performed for the 1-ML system remains valid also for 2 ML.

We emphasize again that at both coverages the values of τ reported above are intended to provide an estimate for the order of magnitude of the simulation time scale, and cannot be interpreted as a fully quantitative measure of the system evolution. Nevertheless, the apparent ability of simulation to reproduce the crucial steps and temperatures characterizing the evolution of the interface support the validity of the computational estimate of energy barriers and therefore of τ.

IX. MAGNETIC PROPERTIES OF THE ANNEALED INTERFACE

The magnetic properties of a sample annealed up to 670 K are compared here to those of the as-deposited layer, and to those of thin Mn layers of different thickness prepared on the same iron surface. The discussion is based on the assumption that a 2×2 MnFe surface alloy forms at the annealed interface, as indicated above by experimental and computational results.

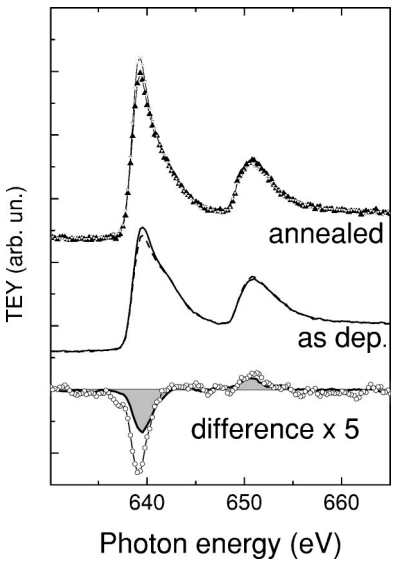

FIG. 13. X-ray-absorption spectra measured in total electron yield for as-deposited 2.5 ML of Mn on the Fe(001) surface (continuous line) and for the same layer annealed to 670 K, resulting in the formation of the stable FeMn surface alloy. The annealed spectrum is multiplied by a constant scaling factor (~ 4) to normalize the measured intensity to the same Mn amount. The XMCD difference curves are reported at the bottom of the figure: the continuous curve and the line plus symbols represent the as-deposited and the annealed interface, respectively.

The Mn magnetic properties are discussed in terms of the XMCD at the $L_{2,3}$ thresholds and the LMDAD of photoelectrons from the $3p$ shell. XMCD can provide an absolute measure of the spin and orbital atomic magnetic moments. The possibility to use the XMCD results for a quantitative determination of both the orbital and spin moments depends on the validity of the sum rules[52] for the XMCD spectra of the $L_{2,3}$ thresholds of Mn. However, the spin-orbit coupling of the Mn $2p$ shell is not large enough to fully separate the two edges in the final state, leading to an error of $\sim 50\%$ on the Mn spin moment evaluation. A correction factor of 1.5 has therefore been suggested in the literature for the Mn spin moment obtained from the sum rules.[35,53] In spite of these problems, XMCD enables us to compare the magnetic properties of the Mn atoms before and after the formation of the alloy. The surface sensitivity of LMDAD provides an independent probe to investigate both the behavior of the Mn atoms and the modification of the Fe atoms properties at the interface.

The XAS and XMCD spectra at the Mn $L_{2,3}$ absorption edges of the 2.5-ML film annealed at 670 K are compared in Fig. 13 with the corresponding spectra recorded for the as-deposited interface. The magnetic signal on the L_3 edge shows that the magnetic moment of the surface alloy is higher than that of the as-deposited film, as confirmed by the values of the spin and orbital magnetic moments reported in Table II, obtained by applying the XMCD sum rules to the

TABLE II. Spin and orbital magnetic moments and maximum asymmetry of LMDAD signal of Mn atoms. The magnetic moments are obtained by applying the XMCD sum rules to the experimental results without including any correction factor. The first three lines refer to as-deposited samples, the last line refers to a sample annealed at $T=670$ K.

Sample	μ_S	μ_L	LMDAD (%)
0.5-ML Mn/Fe(001)	1.5	0.25	12.5
1.3-ML Mn/Fe(001)	0.9	0.15	9
2.5-ML Mn/Fe(001)	0.55	0.05	6
Annealed	0.8	0.2	9

spectra of Fig. 13. To allow an easy comparison with other experimental results, the values reported in the figure and in the table have not been corrected by the 1.5 factor discussed above. In particular, the spin and orbital magnetic moments of the Mn atoms in the surface alloy are both enhanced, reaching values that are similar to those of as-deposited films at 1.3 ML. The branching ratio extracted from the spectra of Fig. 13 for the surface alloy is 0.74, much higher than that of the 0.5-ML coverage (0.71) and of all the as-deposited layers (see Fig. 2).

The Fe and Mn $3p$ photoemission spectra measured in chiral geometry for the as-deposited layer (continuous line) and the alloy (line and symbols) are compared in Fig. 14, while the corresponding LMDAD signals are reported at the bottom of the figure. A comparison of the as-deposited and annealed samples has to take into account that the results refer to different integrated $3p$ intensities. Therefore, while the LMDAD signal of the as-deposited sample is reported directly, the relative variation of the magnetic signal is evaluated after multiplying the LMDAD difference of the annealed sample by the variation of the $3p$ peak total intensity.

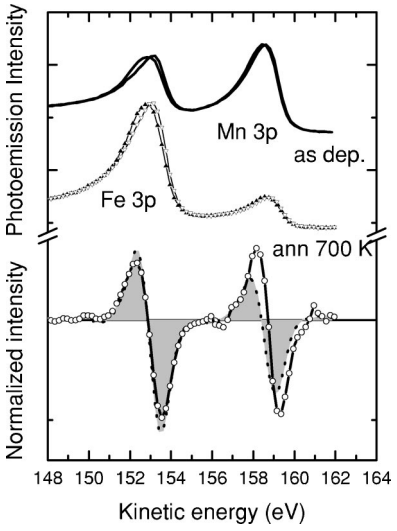

FIG. 14. Photoemission spectra measured with a photon energy of 210 eV for the as-deposited 2.5-ML of Mn on Fe(001) (continuous line) and for the annealed interface (thin line with triangles). In each case, two spectra are recorded upon reversing the magnetization direction in chiral geometry. The LMDAD difference signals are reported at the bottom of the figure. For the as-deposited sample we report directly the difference signal (shaded area with dots), while for the annealed layer the difference signals obtained on the Fe and Mn $3p$ line shapes where normalized independently to the intensity variation of the corresponding core level signal (line with empty circles).

The binding energy of the Mn $3p$ core level shifts towards lower values during the annealing process. This shift of about 200 meV is clearly visible on the comparison of the LMDAD signals at the bottom of Fig. 14. The maximum of the measured LMDAD asymmetry is reported in Table II. The Mn $3p$ LMDAD amplitude for the surface alloy increases by 30% with respect to the as-deposited layer. At the same time, the LMDAD signal amplitude at the Fe $3p$ peak reduces in the alloy by 20% with respect to the iron signal coming from the substrate of the as-deposited sample.

An estimate of the magnetic moment of Fe atoms in the alloy can be obtained by taking advantage of the photoemission surface sensitivity. If we attribute the variation in the LMDAD magnetic signal only to the first and second iron neighbors of manganese, i.e., to the Fe atoms in the 2×2 surface layer and in the first Fe underlayer, we can estimate that the 20% reduction of the LMDAD Fe amplitude corresponds to a decrease of the Fe magnetic moment to $1.1\mu_B$.

These estimates of $0.8\mu_B$ obtained directly for the Mn magnetic moment and of $1.1\mu_B$ for iron in the surface alloy in a ferromagnetic configuration refer to the projection of these moments along the z direction, and could be compatible with different noncollinear magnetic structure. Noncollinear magnetism in MnFe alloys has been recently discussed in Ref. 54.

Unfortunately, only very few experiments are available in the literature on thin-film Mn-Fe alloys. Dechelette *et al.*[27] studied the magnetic properties of $Fe_{0.7}Mn_{0.3}$ and $Fe_{0.9}Mn_{0.1}$ thin films 25 Å thick. At the highest Mn concentration the film adopts a fcc structure, and therefore its properties are not directly comparable to those of the present experiments, in which the alloy is stabilized into the bcc structure by the substrate. At the lowest Mn concentration, however, the film has a bct structure, similar to that of Mn/Fe(001) interfaces. In this case, which is more relevant for our discussion, the moments carried by Mn and Fe atoms are antiparallel. Both species are in a high spin state, with moments of $1.7\mu_B$ and $2.1\mu_B$ for Mn and Fe, respectively. These results differ from those of the present study both for the size of the Mn and Fe magnetic moments, and for the sign of their coupling. The difference can be due to the specific 2×2 arrangement of the surface alloy and to the lateral lattice parameter imposed by the Fe(001) epitaxy.

The scalar relativistic version of the **k**-space tight-binding linear muffin-tin method has been applied both to a 1-ML epitaxial Mn overlayer[21] and to a bilayer of an ordered MnFe alloy[23] on Fe(100). The total Mn coverage of the bilayer is also 1 ML. For the single plane Mn overlayer the more stable configuration is given by an antiferromagnetic Mn layer. This solution is nearly degenerate with a configuration showing a partial ferromagnetic coupling of the Mn surface atoms. Also for the bilayer they obtained that the more stable configuration corresponds to an antiferromagnetic alignment.

A small energy difference was obtained for a more complicated configuration of the magnetic moment characterized by antiparallel alignment of Mn nearest neighbors. Both calculations do not correspond to the stable surface alloy obtained with the annealing process, but suggest the possibility of a ferrimagnetic configuration with two inequivalent Mn sites. This spin arrangement could be consistent with the high BR value and the low XMCD signal of the surface alloy when is compared with the properties of the submonolayer coverage.

Our result ($0.8\mu_B$) for the magnetic moment of Mn atoms in the surface alloy turn out to be close to the moment ($0.77\mu_B$) measured by neutron scattering for Mn impurities in bcc iron.[55] The same system has been studied by KKR computations in Ref. 56, predicting a Mn-Fe ferromagnetic coupling, with a Mn magnetic moment of $\sim 0.7\mu_B$ and a reduction of the moment of the neighboring Fe atoms.

X. SUMMARY AND CONCLUDING REMARKS

Manganese overlayers on the Fe(001) surface have been prepared at room temperature at coverages up to 4.5 ML. Analysis of structural and magnetic properties for the as-deposited samples show that the Mn layer is ferromagnetic up to 2.5 coverage, with a ferromagnetic moment collinear with that of iron. The magnetic moment per Mn atom decreases monotonically with coverage, and layers thicker than ~ 4 ML are antiferromagnetic.

The thermal stability of the interface has been investigated by heating the system at the relatively slow rate of $dT/dt \sim 0.5$ K/s, and monitoring the system evolution by photoelectron spectroscopy. The surface composition is directly measured by the ratio of Mn and Fe PE intensities. The first changes in this ratio are detected at $T = 450$ K, signaling the onset of interdiffusion. The time (and therefore, temperature) evolution of the surface composition displays a plateau for 610 K$\leqslant T \leqslant$680 K, suggesting that a stable or metastable structure is formed in this temperature range. Interdiffusion resumes at higher temperature, as shown by a further decrease of the relative Mn signal.

The structure underlying the plateau in the photoelectron data is identified by means of computer simulations based on a modified embedded atom model. Monte Carlo simulations, in particular, show that starting from Mn overlayers of different thickness ($\geqslant$0.5 ML), a single-layer MnFe surface alloy forms at temperatures comparable to those of the experimental plateau, and displays a 2×2 surface unit cell. On the time scale allowed by the simulation (much shorter than the experimental time scale at high T), the surface alloy is destabilized at temperatures higher than ~ 700 K, leading to full interdiffusion of Mn in the iron substrate.

A surface alloy with an identical 2×2 local arrangement, and lacking long-range order was already observed in the scanning tunneling images of Ref. 15, and investigated by computational means in Ref. 23. It is also worth pointing out that equiatomic surface alloys are known to form also in the case of Mn on several other transition-metal surfaces, including Ni(001) and Cu(001) (see Refs. 57 and 58).

The detailed analysis of electronic and magnetic properties of samples annealed up to ~ 650 K, thus displaying the 2×2 alloy at their surface, show that the alloy plane is ferromagnetic. The measured magnetic moments are $0.8\mu_B$ and $1.1\mu_B$ for Mn and Fe atoms, respectively. The Mn moment is similar in size to the one measured on as-deposited layers at coverage ~ 1 ML. The effects of alloying on the electronic properties is reflected in a shift of 200 meV in the binding energy of the Mn $3p$ core level.

The MEAM scheme used to identify the surface alloy has been also applied for an extensive investigation of energy and kinetic properties of the Mn/Fe(001) interface. The results agree qualitatively with those obtained by a variety of experimental and *ab initio* methods. As-deposited layers, in particular, are epitaxial and planar up to 3-ML coverage. At higher coverages the upper atomic layers are no longer planar, and layer by layer growth turns into layer plus islands for coverages higher than ~ 7 ML.

The demonstrated ability of the model to reproduce at least qualitatively the behavior of the system opens the way to a wide range of new investigations, including the analysis of the role of steps and of localized surface defects, as well as large-scale simulations of the interdiffusion process.

APPENDIX: THE FIT OF THE MEAM POTENTIAL

The MEAM scheme[40] represents a major improvement with respect to the simple EAM,[28] and allows us to reproduce complex structures with many atoms in the unit cell.[41] On the one hand, the enhanced capability of MEAM extends significantly the class of metals and alloys for which the model provides a qualitatively correct description. On the other hand, the flexibility of MEAM is due to a large number of free parameters whose value needs to be tuned on experimental or *ab initio* data. This, in turn, gives rise to a fairly complex fit problem, which represents a challenging step in any MEAM-based simulation.

The number of free parameters in MEAM can be appreciated by listing all the functions entering the MEAM energy expression. The two-body part is given by

$$\varphi_{I,J}(R) = \frac{Z_I(R) Z_J(R)}{R}, \tag{A1}$$

where, in our implementation

$$Z_I(R) = Z_0(1 + b_2 R^2 + b_4 R^4 + b_6 R^6 + b_8 R^8) \times \exp[-\lambda_R(R/R_0 - 1)]. \tag{A2}$$

In the last equation, R_0 is the nearest-neighbor distance in the most representative crystal structure of element I (it simply provides a fixed length scale), and b_2, b_4, b_6, b_8, and λ_R are free parameters.

For what concerns the atomiclike densities, we took

$$\rho^{(0)}(R) = t_0 \left(\frac{R}{R_0}\right)^{\nu} \exp[-\lambda_0(R/R_0 - 1)] \tag{A3}$$

and

$$\rho^{(i)}(R) = t_0 \exp[-\lambda_i(R/R_0 - 1)]. \tag{A4}$$

TABLE III. Properties of bcc Fe and α-Mn as computed by the present MEAM model. The available experimental data are reported in parenthesis. In addition to the lattice constant a_0 and cohesive energy E_0, the table reports the bulk modulus B, the elastic constants C_{11}, C_{12}, C_{44}, the vacancy formation energy E_v^f, the energy of the (001) surface, and the frequency ω of phonons at $\mathbf{K}=2\pi/a$ (0.5,0.5,0.5).

	a_0 (Å)	E_0 (eV)	B (Mbar)	C_{11} (Mbar)	C_{12} (Mbar)	C_{44} (Mbar)	E_v^f (eV)	σ_{001} (dyn/cm^2)	$\omega(\mathbf{K}=0.5,0.5,0.5)$ (THz)
Fe	2.8665	4.28	1.683	2.10	1.47	0.675	2.10	2480	7.48
	(2.8665)	(4.28)	(1.683)	(2.431)	(1.381)	(1.219)	(1.79)		7.20
Mn	8.894	2.902	1.210	1.98	0.827	0.747	1.20	1499	
	(8.894)	(2.902)	(1.210)						

In the equations above, t_0, $\lambda_i, i=0,\ldots,3$, and ν are free parameters. Additional free parameters are given by $(t_i,s_i), i=1,3$ coefficients entering Eq. (3) in Sec. IV.

In full analogy with what is done in EAM, all but one (t_0) of the parameters are tuned on properties of each element. Only t_0 is used to adjust the cross interaction in alloys. Again in analogy with the standard EAM case, it is possible to identify exact or approximate relations between specific properties and subsets of the free coefficients, thus allowing a pre-selection of the potential, leaving only the final refinement stage to the full unconstrained optimization.

In the case of iron, the parameters have been selected in order to reproduce the energy versus pressure ($T=0$) equation of state,[59] elastic constant, vacancy formation energy, and (001) surface energy of α-Fe (bcc), as well as the frequency of zone-boundary phonons for the same phase. With this potential, the fcc (γ-Fe) phase has a higher potential energy per atom, a slightly larger equilibrium volume, and a lower bulk modulus, but we did not investigate directly the $\alpha \rightarrow \gamma$ transition. We only verified that the α phase is stable up to the temperatures of interest for the present study ($T \sim 800$ K). The comparison of computed and experimental properties for pure iron is carried out in Table III.

In the case of manganese, the choice of experimental data to be reproduced by the potential is both more restricted and more uncertain. The $T=0$ energy vs pressure equation of state, for instance, displays a number of anomalies due to magnetic transition in elemental Mn under pressure.[60] The zero-pressure bulk modulus, measured by ultrasonic experiments,[61] is $B_0=93$ GPa. A fit of the experimental equation of state under pressure, however, provides results for B_0 and B' (pressure derivative of the bulk modulus) strongly dependent on the pressure range that is considered. We expect Mn to experience sizable strain in mixing with iron, and therefore we reproduce by our model the equation of state reported in Ref. 60 and valid up to 20 GPa ($B_0=121$ GPa, $B'=7.4$ GPa). Phonons and elastic constants are not readily available in the literature, moreover, they are affected by large uncertainties, and, in any case, they would not be fully consistent with our choice of B_0 and B'. For these reasons, we use in our fit the same elastic constants of iron, scaled by the ratio of the bulk moduli B_0 for Mn and for Fe, and we do not include any requirement on phonons. Instead, we fit the ground-state geometry of α-Mn, and the energy of the (001) surface. The comparison of experimental and computed properties is reported in Table III. The cross interaction between Fe and Mn has been adjusted by changing the t_0 parameter of Fe with respect to the value set for Mn. The lattice parameter and mixing enthalpy of random solid solutions of Mn in α-Fe (with manganese concentrations of up to 10 at. %) have been used to select a value of $t_0=0.42$ for Fe, keeping fixed $t_0=1$ for Mn.

The clean Fe(001) surface displays little relaxation, in agreement with experimental data.[62]

The full set of parameters, the program to compute the embedding functions, and the simulation programs are available from the authors.

*Corresponding author. Electronic address: fausto.sirotti@lure.u-psud.fr

[1] H. Dreysse and C. Demangeat, Surf. Sci. Rep. **28**, 65 (1997).
[2] C. Demangeat and J.C. Parlebas, Rep. Prog. Phys. **65**, 1679 (2002).
[3] The moment is reduced to $0.65\mu_B$ in the antiferromagnetic α-Mn phase.
[4] S.K. Nayak and P. Jena, Chem. Phys. Lett. **289**, 473 (1998).
[5] S. Blügel, M. Weinert, and P.H. Dederichs, Phys. Rev. Lett. **60**, 1077 (1988); S. Blügel and P.H. Dederichs, Europhys. Lett. **9**, 597 (1989).
[6] S.K. Kim, Y. Tian, M. Montesano, F. Jona, and P.M. Marcus, Phys. Rev. B **54**, 5081 (1996).
[7] O. Rader, W. Gudat, D. Schmitz, C. Carbone, and W. Eberhardt, Phys. Rev. B **56**, 5053 (1997).
[8] T. Igel, R. Pfandzelter, and H. Winter, Phys. Rev. B **58**, 2430 (1998).
[9] T.G. Walker and H. Hopster, Phys. Rev. B **48**, 3563 (1993).
[10] Ch. Roth, Th. Kleemann, F.U. Hillebrecht, and E. Kisker, Phys. Rev. B **52**, R15 691 (1995).
[11] S. Andrieu, M. Finazzi, F. Yubero, H. Fischer, P. Arcade, F. Chevrier, H. Hricovini, G. Krill, and M. Piecuch, J. Magn. Magn. Mater. **165**, 191 (1997).
[12] S. Andrieu, M. Finazzi, Ph. Bauer, H. Fischer, P. Lefevre, A. Traverse, K. Hricovini, G. Krill, and M. Piecuch, Phys. Rev. B **57**, 1985 (1998).
[13] T.K. Yamada, M.M.J. Bischoff, T. Mizoguchi, and H. van Kempen, Surf. Sci. **516**, 179 (2002).
[14] R. Pfandzelter, T. Igel, and H. Winter, Surf. Sci. **389**, 317 (1997).
[15] M.M.J. Bischoff, T.K. Yamada, A.J. Quinn, and H. van Kempen, Surf. Sci. **501**, 155 (2002).
[16] J. Dresselhaus, D. Spanke, F.U. Hillebrecht, E. Kisker, G. van der

Laan, J.B. Goedkoop, and N.B. Brookes, Phys. Rev. B **56**, 5461 (1997).
[17] S. Andrieu, E. Foy, H. Fischer, M. Alnot, F. Chevrier, G. Krill, and M. Piecuch, Phys. Rev. B **58**, 8210 (1998).
[18] B. Nonas, K. Wildberger, R. Zeller, and P.H. Dederichs, J. Magn. Magn. Mater. **165**, 137 (1997).
[19] B. Nonas, K. Wildberger, R. Zeller, and P.H. Dederichs, Phys. Rev. Lett. **80**, 4574 (1998).
[20] R. Wu and A.J. Freeman, Phys. Rev. B **51**, 17 131 (1995).
[21] O. Elmouhssine, G. Moraitis, C. Demangeat, and J.C. Parlebas, Phys. Rev. B **55**, R7410 (1997).
[22] S. Handschuh and S. Blügel, Solid State Commun. **105**, 633 (1998).
[23] M. Taguchi, O. Elmouhssine, C. Demangeat, and J.C. Parlebas, Phys. Rev. B **60**, 6273 (1999).
[24] S. Bouarab, H. Nait-Laziz, M.A. Khan, C. Demangeat, H. Dreyssé, and M. Benakki, Phys. Rev. B **52**, 10 127 (1995).
[25] T. Asada, S. Blügel, G. Bihlmayer, S. Handschuh, and R. Abt, J. Appl. Phys. **87**, 5935 (2000).
[26] T. Igel, R. Pfandzelter, and H. Winter, Surf. Sci. **405**, 182 (1998).
[27] Magnetic properties of strained Fe_xMn_{1-x} thin films have been investigated by A. Dechelette, M.C. Saint-Lager, J.M. Tonnerre, G. Patrat, D. Raoux, H. Fischer, S. Andrieu, and M. Piecuch, Phys. Rev. B **60**, 6623 (1999); **60**, 6636 (1999).
[28] M.S. Daw and M.I. Baskes, Phys. Rev. Lett. **50**, 1285 (1983); Phys. Rev. B **29**, 6443 (1984).
[29] F. Sirotti, F. Polack, J.L. Cantin, M. Sacchi, R. Delaunay, and M. Liberati, J. Synchrotron Radiat. **7**, 5 (2000).
[30] F. Sirotti and G. Rossi, Phys. Rev. B **49**, 15 682 (1994).
[31] C.T. Chen, Y.U. Idzerda, H.-J. Lin, N.V. Smith, G. Meigs, E. Chaban, G.H. Ho, E. Pellegrin, and F. Sette, Phys. Rev. Lett. **75**, 152 (1995).
[32] G. Panaccione, F. Sirotti, and G. Rossi, Solid State Commun. **113**, 378 (2000).
[33] B.T. Thole and G. van der Laan, Phys. Rev. B **38**, 3158 (1988).
[34] O. Rader, C. Pampuch, W. Gudat, A. Dallmeyer, C. Carbone, and W. Eberhardt, Europhys. Lett. **46**, 231 (1999).
[35] H.A. Dürr, G. van der Laan, D. Spanke, F.U. Hillebrecht, and N.B. Brookes, Phys. Rev. B **56**, 8156 (1997).
[36] J.J. Yeh and I. Lindau, At. Data Nucl. Data Tables **32**, 1 (1985).
[37] S.M. Foiles, M.I. Baskes, and M.S. Daw, Phys. Rev. B **33**, 7983 (1986).
[38] V. Rosato, M. Guillopé, and B. Legrand, Philos. Mag. A **59**, 321 (1989); F. Cleri and V. Rosato, Phys. Rev. B **48**, 22 (1993).
[39] M.I. Haftel, T.D. Andreadis, J.V. Lill, and J.M. Eridon, Phys. Rev. B **42**, 11 540 (1990).
[40] M.I. Baskes, Phys. Rev. Lett. **59**, 2666 (1987); M.I. Baskes, J.S. Nelson, and A.F. Wright, Phys. Rev. B **40**, 6085 (1989); M.I. Baskes, *ibid.* **46**, 2727 (1992).
[41] B.-J. Lee and M.I. Baskes, Phys. Rev. B **62**, 8564 (2000).
[42] M.P. Allen and D.J. Tildesley, *Computer Simulation of Liquids* (Clarendon, Oxford, 1989).
[43] One pair interchange is attempted every 3000 single atom moves.
[44] A.F. Voter, Phys. Rev. B **34**, 6819 (1986).
[45] N. Papanikolaou, B. Nonas, S. Heinze, R. Zeller, and P.H. Dederichs, Phys. Rev. B **62**, 11 118 (2000).
[46] *Order and Phase Stability in Alloys*, edited by F. Ducastelle (North-Holland, Amsterdam, 1991).
[47] A. Christensen, A.V. Ruban, P. Stoltze, K.W. Jacobsen, H.L. Skriver, and J.K. Norskov, Phys. Rev. B **56**, 5822 (1997).
[48] Slight fluctuations in the results of Fig. 7 are due to the random choice of the atom pairs to be exchanged.
[49] More precisely, the alloy structure should be identified as $\sqrt{2} \times \sqrt{2}$.
[50] Preliminary results using a larger sample (6912 atoms) and a simulation cell commensurate with the 2×2 surface unit cell confirm the results presented in Sec. VII: the 2×2 reconstruction is the only recognizable feature in the surface structure, but its order is limited to relatively short range (up to $\sim$10 Å).
[51] T. Mülders, P. Krüger, W. Swegat, and J. Schlitter, J. Chem. Phys. **104**, 4869 (1996).
[52] B.T. Thole, P. Carra, F. Sette, and G. van der Laan, Phys. Rev. Lett. **68**, 1943 (1992).
[53] Y. Tanemura, A. Tanaka, and T. Jo, J. Phys. Soc. Jpn. **65**, 1053 (1996)
[54] K. Nakamura, T. Ito, A.J. Freeman, L. Zhong, and J. Fernandez-de-Castro, Phys. Rev. B **67**, 014405 (2003).
[55] P. Radhakrisna and F. Livet, Solid State Commun. **25**, 597 (1978).
[56] B. Drittler, N. Stefanou, S. Blügel, R. Zeller, and P.H. Dederichs, Phys. Rev. B **40**, 8203 (1989).
[57] M. Wuttig, Y. Gauthier, and S. Blügel, Phys. Rev. Lett. **70**, 3619 (1993).
[58] W.L. O'Brien and B.P. Tonner, Phys. Rev. B **51**, 617 (1995).
[59] P. Vinet, J.R. Smith, J. Ferrante, and J.H. Rose, Phys. Rev. B **35**, 1945 (1987).
[60] H. Fujihisa and K. Takemura, Phys. Rev. B **52**, 13 257 (1995).
[61] M. Rosen, Phys. Rev. **165**, 357 (1968).
[62] K.O. Legg, F. Jona, D.W. Jepsen, and P.M. Marcus, Surf. Sci. **66**, 25 (1977); H. Ohtani, Prog. Surf. Sci. **23**, 155 (1986); G. Panzner, Surf. Sci. **133**, 651 (1984).